





Extrinsic room-temperature ferromagnetism in MoS₂

Sabyasachi Saha^{1,2,*} , Manuel Bañobre-López³, Oleksandr Bondarchuk⁴, Joaquín Fernández-Rossier⁵, and Francis Leonard Deepak^{1,*} 

¹Nanostructured Materials Group, International Iberian Nanotechnology Laboratory, Av. Mestre José Veiga, 4715-330 Braga, Portugal

²Electron Microscopy Group, Defence Metallurgical Research Laboratory, Hyderabad 500058, India

³Advanced (magnetic) Theranostic Nanostructures Lab - Nanomedicine Group, International Iberian Nanotechnology Laboratory (INL), Av. Mestre José Veiga, 4715-330 Braga, Portugal

⁴Advanced Electron Microscopy Imaging and Spectroscopy, International Iberian Nanotechnology Laboratory (INL), Av. Mestre José Veiga, 4715-330 Braga, Portugal

⁵QuantaLab, International Iberian Nanotechnology Laboratory (INL), Av. Mestre José Veiga, 4715-330 Braga, Portugal

Received: 30 September 2020

Accepted: 8 February 2021

Published online:

2 March 2021

© The Author(s), under exclusive licence to Springer Science+Business Media, LLC part of Springer Nature 2021

ABSTRACT

We report stable room-temperature ferromagnetism in commercially available MoS₂ powder with a nominal purity greater than 98%. In order to assess the origin of the unexpected ferromagnetic signal, we carried out thorough characterization of the samples, by a combination of X-ray diffraction, Raman spectroscopy, electron microscopy, X-ray photoelectron spectroscopy and superconducting quantum interference device magnetometry. Using secondary ion mass spectrometry, we infer that up to 1.6% of a pool of different external dopants, including 0.8% of Fe and others, are present in the MoS₂ samples. We find very low value of magnetic moment per unit formula that, together with the small density of magnetic dopants, and the room-temperature magnetic order, leads us to conclude that ferromagnetism is not hosted at the MoS₂ crystal but can be ascribed to secondary phase of transition metal atoms' clusters that aggregate. Our results stress the need of a careful characterization of transition metal dichalcogenides in the study of magnetism and spintronics involving either nominally pure MoS₂ as a diamagnetic semiconductor substrate or as a host material for diluted magnetic alloying.

Handling Editor: Yaroslava Yingling.

Address correspondence to E-mail: saha.sabyasachi@gmail.com; leonard.francis@inl.int

Introduction

Semiconductors, which have no unpaired spins, do not exhibit ferromagnetism, since the dominant contribution to the magnetic response in those materials come from orbital response. MoS₂ is one such compound, which is diamagnetic and is very well-known layered semiconductor compound that has been studied extensively, both in bulk and in its 2D form [1–3]. 2H-MoS₂ is known to be a diamagnetic semiconductor, with the absence of unpaired spins, with a very strong spin–orbit coupling and, in the 2D case, with a strong spin-valley coupling [4] that permits to induce optical orientation [5, 6], i.e. the induction of a net spin polarization in response to spin polarized light. The fact that low energy bands of 2D materials can be described in terms of a massive Dirac equation, and the huge spin splitting of their valence band [4] and a sizable splitting of the conduction band [7], has elicited a huge attention in the last decade. Importantly, the origin of spin splitting is the combination of spin orbit coupling and lack of inversion symmetry, different from exchange-induced splitting in materials with magnetic order.

Recently, there is very strong interest in magnetically ordered 2D crystals [8, 9], triggered by the observation of ferromagnetic order in a monolayer of CrI₃, a layered ferromagnetic semiconductor [10]. This has been followed by the analogous finding in other compounds, layered magnetic crystals, such as (CrGeTe, CrBr₃, CrCl₃, VI₃, CrTe₂, FeGeTe) [11–16]. Interest in these materials is further increased by the fact that some of these have demonstrated applications in various spin logic device technologies [17], but the use of these materials for many potential applications gets reduced by the fact that, in most instances, their magnetic order vanishes at room temperature.

An alternative route to obtain functional magnetic 2D materials may come from magnetic alloying of 2D semiconductors, such as MoS₂. The so-called diluted magnetic semiconductors were intensively studied in the case of conventional II-VI and III-V semiconductors [18–21] and inspired the birth of the field of spintronics [22, 23]. However, the quest for a material that has both ferromagnetic order at room temperature and operates like a functional semiconductor with field effect control of its conductance still remains a challenge [20, 21]. Importantly, additional

functionality would only arise if the same carriers that participate in transport are affected by the magnetic order.

Ferromagnetic order was reported in nominally undoped MoS₂, and it was attributed to edge magnetism [24–26] and to sulphur vacancies [27]. Transformation to 1 T-polytype may also lead to magnetic ordering [28]. This has also been demonstrated as a result of vacancy-induced ferromagnetism by creation of subdomains of the 1 T-polytype [29]. Ferromagnetic behaviour has recently been reported in naturally diamagnetic MoS₂ by doping with Mn, Fe and Co or other dopant elements [30–32]. Enhanced magneto-optical response has also been reported recently in Fe-doped MoS₂ monolayers [33]. Interest in magnetic order in transition metal dichalcogenides, includes also vanadium-doped WSe₂ [34–36] and WS₂ [37], as well as a report on defect-induced ferromagnetism in 2H-MoTe₂ and 2H-MoSe₂ [38].

Doping in MoS₂ has been reported for different dopant atoms, and multiple fabrication techniques are employed to achieve this by several groups [33, 39–47]. Most of these studies have focussed mainly on optical and electronic properties, whereas only a few of them have reported about the desired property of magnetism, especially realization of room-temperature ferromagnetism which is yet to mature.

Here we report the existence of room-temperature ferromagnetism in commercially acquired MoS₂ materials. As we will show below, we attribute this finding to the existence of a secondary phase of magnetic impurities, and we highlight the importance of careful characterization when unexpected magnetism is found, stressed in previous works [48, 49]. Specifically, in this work we make use of advanced characterization techniques such as X-ray diffraction (XRD), Raman spectroscopy, X-ray photoelectron spectroscopy (XPS), secondary ion mass spectrometry (SIMS) and aberration-corrected transmission electron microscopy in order to understand their microstructure and conclude that magnetism in our samples is extrinsic.

Experimental

Our samples were obtained from several leading suppliers, namely Sigma-Aldrich and American Elements. Samples 1 and 2 are MoS₂ samples from

Sigma-Aldrich (Product # 804,169 and Product # 234,842), with a quoted average particle size (APS) of 90 nm and $< 2 \mu\text{m}$ with 99% and 98% purity, respectively. Sample 3 is MoS_2 sample from American Elements (Product code: Mo-S-03 M-PUF.150 N), having APS $< 150 \text{ nm}$ with 99.9% purity.

XRD diffraction analysis was carried out using PANalytical make X'PERT PRO MRD X-Ray diffraction system, in the Bragg Brentano configuration for powder analysis by the θ – 2θ scans. It has been performed by sticking the sample on a holder using a glue which gives a known peak at 27.9 in the 2θ scan. Raman spectroscopy was performed using the WITec make Alpha300M+ Raman spectrometer using the 532 nm laser and 1800 grating, providing a spectral resolution better than 1 cm^{-1} .

X-Ray Photoelectron Spectroscopy (XPS) system ESCALAB 250Xi from Thermo Scientific was employed in order to understand the chemical nature of the samples. Mass spectra of the samples was obtained by using a time-of-flight secondary ion mass spectrometry (TOF-SIMS) system, TOF-SIMS4 from ION-TOF GmbH with a single stage reflector design. Bi^{3+} was used as the primary ion source at 25 kV with a cycle time of 150 μs on an analysis area of $500 \times 500 \mu\text{m}^2$.

The magnetic response of the samples has been characterized using the superconducting quantum interference device (SQUID) magnetometer, MPMS-SQUID-VSM from Quantum Design. The powder samples were placed in gelatine capsules and introduced in a straw holders. These holders were subsequently attached to the squid rod sample holder and loaded in the squid. Hysteresis loops were acquired as a function of the applied magnetic field up to 20 kOe at 300 and 5 K. Magnetization curves as a function of the temperature in the range 5–300 K were acquired under zero-field-cooling and field cooling (ZFC–FC) conditions at a magnetic field of 0.1 kOe.

The structural analysis was carried out using transmission electron microscopy. Samples for TEM were prepared by bath sonicating the sample powder in ethanol for 20 min and subsequently drying few drops of the solution on carbon-coated Cu grids. The samples have been imaged using a probe-corrected FEI Titan G² ChemiSTEM and double corrected FEI TITAN Themis TEMs (point resolution better than 80 pm in the TEM and STEM modes at 200 kV accelerating voltage) equipped with a Super-X EDX

System, which comprises of four windowless silicon drift detectors of 120 mm^2 size and having an overall energy resolution better than 140 eV. The samples were imaged both in TEM and STEM modes as well as analysed using STEM-EDS. The EDS data are acquired and analysed using the Bruker QUANTAX Esprit 1.9 software. The quantification was obtained using the Cliff-Lorimer Method. Electron energy loss spectra (EELS) was acquired using the probe-corrected FEI Titan ChemiSTEM at 200 kV equipped with a Gatan GIF spectrometer.

Results and discussion

X-ray diffraction (XRD) from all the samples confirms the presence of 2H- MoS_2 crystallographic phase, ruling out the formation of 1T-polytype for which ferromagnetism has been predicted [28]. The crystallite size is also calculated using the Scherrer's equation, and it is estimated to be $\sim 90 \text{ nm}$, $\sim 60 \text{ nm}$ and $\sim 9 \text{ nm}$ for sample 1, sample 2 and sample 3, respectively, under the assumption that peak broadening is due to the crystal size alone. It needs to be mentioned that these calculated sizes may be different from the actual particle sizes, and are noted to be different from the quoted values. The Raman spectroscopy results also suggest the same with characteristic peaks E_{2g}^1 at 376 cm^{-1} and A_{1g} at 402 cm^{-1} . This is also in line with the X-ray photoelectron spectroscopy (XPS) data, which also showed the $\text{Mo}3d_{5/2}$ and $\text{S}2p_{3/2}$ standard peaks for the three samples, without any detectable variations. Similar results were also observed in the electron energy loss spectroscopy (EELS) for the samples. Complete data can be referred in the Supplementary Information.

Figure 1 shows the magnetic hysteresis loops for the different samples. The magnetic moment (in milli-Bohr magneton (mBM)) is plotted versus the applied magnetic field for samples 1, 2, and 3 at both 5 K and 300 K and shown in Fig. 1a and b, respectively. Sample 1 shows ferromagnetic (FM) behaviour with a superimposed paramagnetic (PM) contribution. The superimposed PM contribution is only visible at low temperature, on account of the $1/T$ scaling of the spin susceptibility for paramagnets. Both coercivity and remanence are observed at both 5 K and 300 K, strongly indicating the presence of

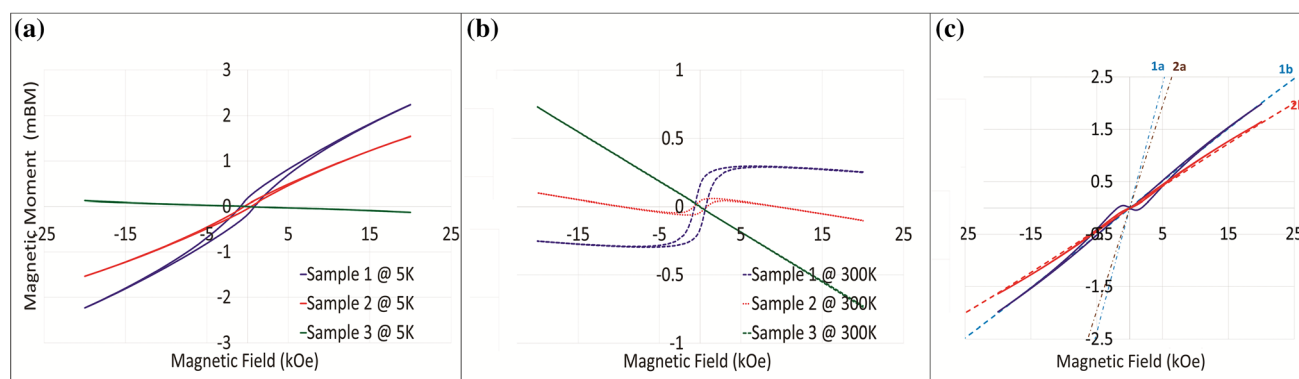


Figure 1 a M-H curves for samples 1, 2 and 3 at 5 K and **b** M-H curves for samples 1, 2 and 3 at 300 K; **c** PM contribution of samples 1 and 2 extracted by subtraction of magnetic moment at 300 K from the one at 5 K, shown by solid lines (blue and red) for samples 1 and 2, respectively. Calculated PM (Brillouin function) plots, indicated by dashed lines 1a, 2a for samples 1 and

ferromagnetic order with a saturation magnetization of about 0.25 mBM in the sample.

Sample 2 is observed to behave similar to sample 1, but the FM contribution at room temperature is lower having saturation magnetization of about 0.05 mBM and an additional diamagnetic (DM) contribution, which is observed as the magnetic field increases.

For Sample 3, the magnetic curve indicates a purely DM state at room temperature, but as the temperature is decreased, a very tiny (~ 0.005 mBM at 1 kOe) PM contribution seems to appear.

Samples 1 and 2 are noted with saturation magnetic moment of about 0.25 mBM and 0.05 mBM per unit formula, respectively. For samples 1 and 2, the PM contribution has been extracted and is shown in Fig. 1c by subtracting the magnetic moment at 300 K from the one at 5 K and is represented by the blue and red solid curves for samples 1 and 2, respectively. The samples exhibiting FM behaviour were further studied as a function of temperature under zero-field-cooled (ZFC)–field-cooled (FC) conditions at fixed magnetic field of 100 Oe. The temperature-dependent magnetic curves showed a decrease in the magnetic moment with increasing temperature, as expected for a regular FM material. For completeness, the data are available in the Supplementary Information (see Fig. SI.5).

Further microstructural studies have been carried out using high-resolution S/TEM and corresponding analytical techniques for the samples 1, 3 (as representative examples from the different magnetic behaviours observed).

2, respectively (moments calculated as per the dopant concentration derived from TOF–SIMS), assuming all dopants have $S = 1/2$ and $g = 2$. 1b and 2b are estimated Brillouin function plots, if the moments/volume is reduced by a factor of 5.4 for sample 1 and 4.2 for sample 2.

Figure 2a shows that the sample 1 is in the form of thin flakes with sizes ranging up to few hundred nanometres and having sharp hexagonal faceted edges. Figure 2b shows the STEM-HAADF micrograph of the flakes and its corresponding energy-dispersive spectroscopy (EDS) maps showing the presence of Mo, S and Fe as indicated by red, green and purple colours, respectively. Figure 2c shows a pseudo-coloured STEM-HAADF micrograph with variation of greyscale intensity of a region of sample 1, revealing hexagonal symmetry. Intensity profile along the line AB in Fig. 2c is also illustrated in a separate inset in the figure indicating the visible doublets along the line. The separation between the doublets is determined to be 1.8 \AA , which matches with the position of atoms for 2H-MoS₂ viewed along [001]. Magnified view of a small area is depicted as an inset, with a simulated projected crystal model of 2H-MoS₂ along the [001] direction superimposed on it. The simulated crystal model is shown by Mo and S atoms in blue and yellow colours, respectively. The presence of Fe in Sample 1 was also noted from the electron energy loss spectroscopy (EELS) spectra shown in Fig. 2d with an edge corresponding to the L₃ edge of Fe at 708 eV as well as from the X-ray photoelectron spectroscopy (XPS) study shown in Fig. 2e, revealing the Fe 2p peaks. This has further been confirmed from time-of-flight secondary ion mass spectroscopy studies, presented in Table 1 for sample 1.

Figure 3 shows that sample 3 is in the form of curled up agglomerates as noted from low-

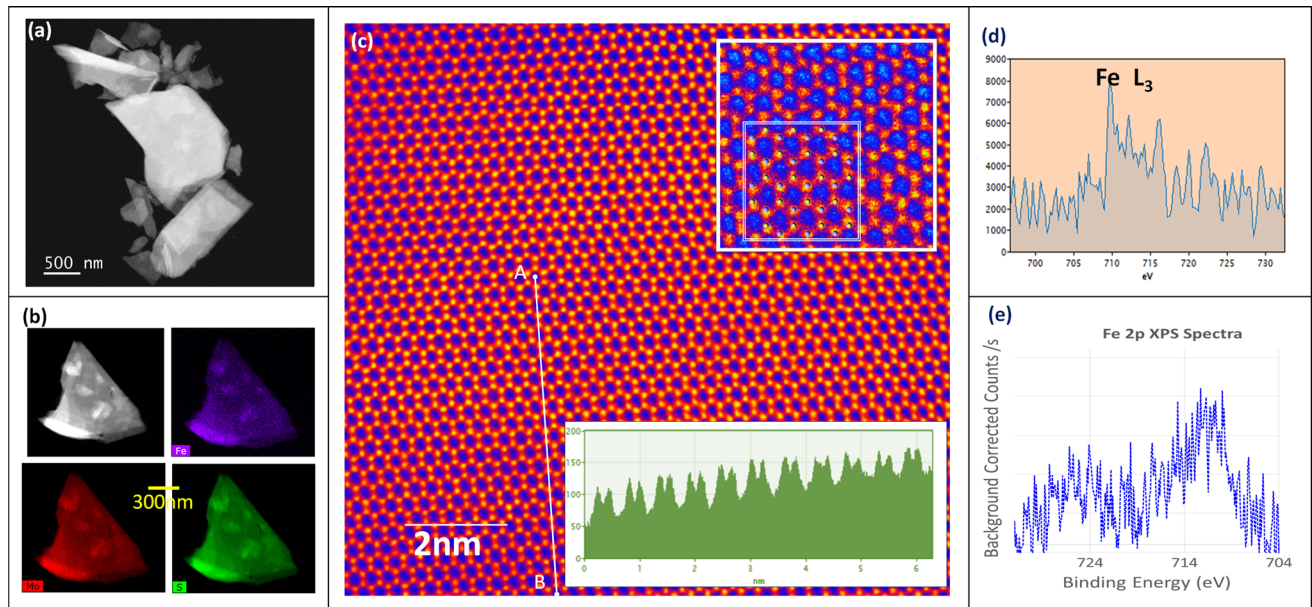


Figure 2 Results from Sample 1: **a** low-magnification STEM-HAADF micrograph, **b** STEM-HAADF micrograph and corresponding EDS mapped images with Fe, Mo and S shown in purple, red and green, respectively, **c** showing pseudo-coloured intensity mapped STEM-HAADF micrograph with the insets

showing a magnified view with the superimposed simulated 2H-MoS₂ and the other showing the intensity profile along the marked line AB, **d** EELS spectra acquired from sample 1 showing the L₃ edge of Fe. And **(e)** XPS spectra of Sample 1 showing the Fe 2p peaks.

Table 1 Chemical composition relative to the Mo concentration in the samples 1, 2, and 3

	Li	Na	Mg	Al	Si	K	Ca	Cr	Mn	Fe	Co	Ni	Cu	Mo
Sample 1	–	11.228	–	0.591	1.030	16.763	0.329	0.021	0.086	0.739	–	–	0.102	100.000
Sample 2	–	6.664	–	0.172	0.262	20.479	0.106	0.013	0.117	0.463	–	–	0.056	100.000
Sample 3	0.054	0.227	0.546	–	0.487	–	0.019	–	0.011	0.043	0.012	0.032	0.120	100.000

magnification micrographs, and made up of individual small curled features, noted from Fig. 3a. Figure 3a shows the STEM-HAADF micrograph, with an array of parallel linear features, corresponding to the layers of the MoS₂. Intensity profiles across them are shown for two marked regions with the inter-planar spacing observed to be ~ 6.2 Å which matches with the inter-planar spacing of 2H-MoS₂ along the [001] direction. Figure 3b shows a STEM-HAADF micrograph of a portion of Sample 3. The corresponding EDS maps show the presence of Mo, which has been indicated by red colour, whereas that of S has been indicated by green. Importantly, the presence of any other elements was not noted (within the detection levels of either the EDS or XPS techniques). Figure 3c shows a STEM-HAADF micrograph at relatively high magnification showing planar periodicities in certain directions. The fast

Fourier transform (FFT) shown as inset confirms this observation, and the micrograph is found to match with the MoS₂ crystal structure (3.160 Å corresponding to the Mo-Mo interatomic distance, when imaged along the [001] direction). Figure 3d and e shows noise filtered micrographs at higher magnification of some of the other different regions of the sample 3 as imaged along the [001] direction. Crystal model projection of 2H-MoS₂ along [001] direction is superimposed on them, with blue and yellow colours depicting Mo and S atoms, respectively.

TEM micrographs showed curled up intertwined layers of MoS₂ for sample 3, in contrast to the large flakes with sharp linear faceted boundaries for sample 1, also evident from the broadened XRD peaks for sample 3 resulting from the lack of long range ordering. All observations from all the studied samples using all the techniques such as Raman, XRD,

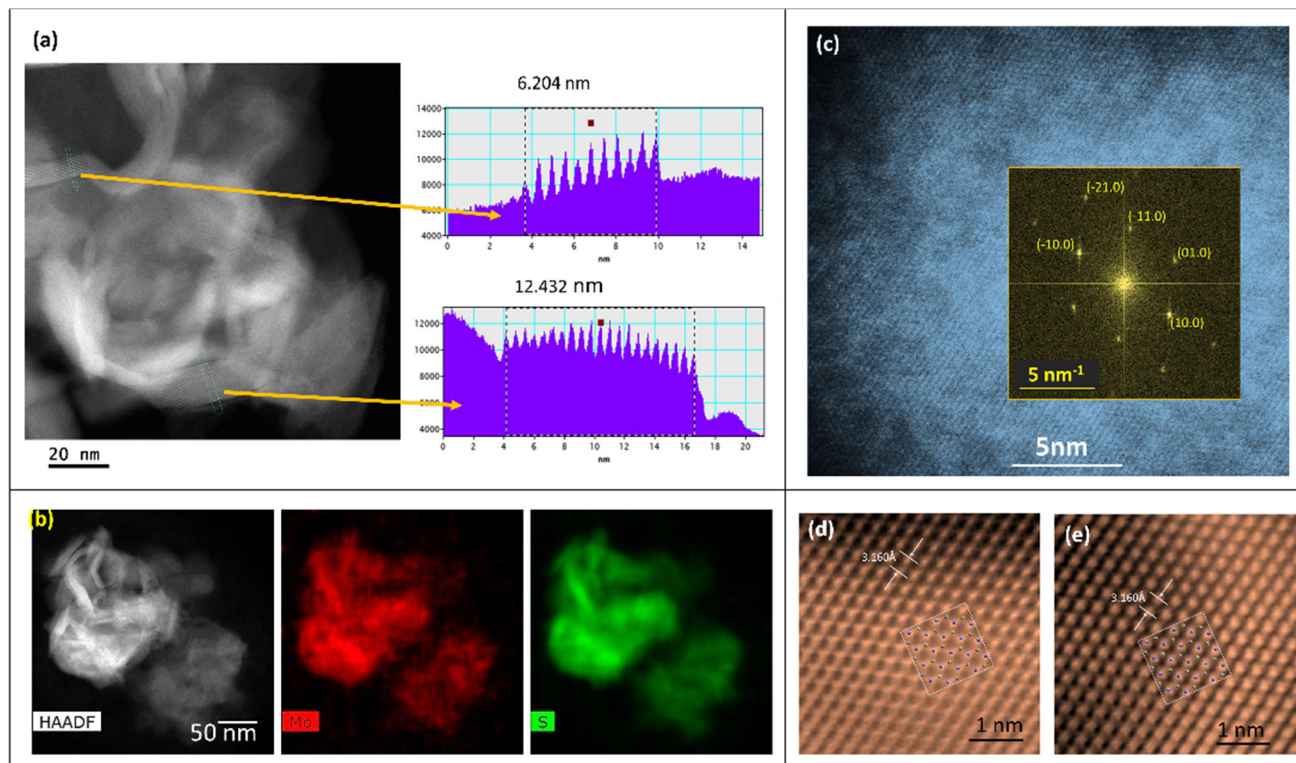


Figure 3 S/TEM results of Sample 3: **a** showing low-magnification STEM-HAADF micrograph with intensity profiles depicting the (002) inter-planar distances along the $\langle 001 \rangle$ - direction; **b** HAADF micrograph along with EDS mapped images with Mo and S shown in red and green, respectively; **c** high-

magnification STEM-HAADF micrograph with its FFT shown in the inset; **d** and **e** showing filtered micrographs of two different regions at higher magnification along with simulated crystal model of 2H-MoS₂ superimposed and inter-planar distance marked.

XPS and TEM unequivocally confirmed to match with the MoS₂ phase.

Compilation of the findings of the chemical analysis using SIMS technique is summarized in Table 1. XPS and EELS for sample 1 had indicated the presence of some Fe, which is also confirmed with higher confidence and measurement accuracy from the TOF-SIMS. From the TOF-SIMS analysis, some additional notable quantities of Al, Mn, Fe and Cu are confirmed in the samples 1 and 2 in addition to the Mo along with significant amounts of Na and K too. Most likely sources of these seem to be the starting precursor materials such as Na₂MoO₄ or K₂MoO₄, which are generally used for synthesis of MoS₂ by hydrothermal techniques [50]. Na and K are highly reactive and are not expected to be in the metallic form, but rather would be in the form of either oxides, hydroxides or halides, and more importantly none of them are known to have any magnetic influences too. It is important to point out that sample 3 is comparatively purer and no notable impurities

are observed. No significant chemical shifts have been observed in the binding energy peaks of the XPS spectra, as well as the edge shifts in EELS, suggesting that the impurities may be present as a secondary phase.

Samples 1 and 2 demonstrated FM behaviour at both low and room temperature, with a superimposed PM contribution. Given the well-established DM nature of MoS₂, ferromagnetism could arise from two sources: edge magnetism [24–26] and point defects, such as vacancies [29] or dopants. We analyse first edge magnetism. Let us for argument sake, assume the most favourable case of triangular-shaped MoS₂ islands with zigzag edges. A flake of with N atoms has roughly \sqrt{N} atoms in the edge. Assuming a magnetic moment of 2 Bohr magneton per edge atom, this would give a small magnetization of the order $1/\sqrt{N}$. Considering samples 1 and 2, with flakes with their quoted size of about 100 nm and 1000 nm lateral dimensions, we estimated the number of edge atoms to be about 300 and 3000, leading to

60 mBM and 6 mBM for the two samples, respectively, roughly compatible with the observed saturation magnetic moment for the two samples, but this type of magnetic behaviour is not expected to be robust and stable up to room temperatures, contrary to what we have observed. Moreover edges are expected to be highly reactive and may not exist with dangling bonds and might be decorated with other atoms such as oxygen. For sample 3 with a quoted average particle size of about 150 nm or smaller, it will lead to high values of magnetization, but this interpretation is incompatible as it shows DM behaviour. Instead, there seems to be a correlation between the observed saturation magnetization and the presence of impurities in the samples. In particular, sample 3 does not contain any significant impurity elements and shows a DM behaviour, as expected for pure MoS₂.

We now consider the other source of the magnetism that is related to sulphur vacancies [29], and it is seen that if vacancies are formed, it leads to local change in microstructure from the 2H-polytype to the 1T-polytype. In our study of sample 1, we did not notice any structural defects over large areas as seen in the STEM-HAADF micrograph in Fig. 2c and presence of local transformations to 1T-polytype due to sulphur vacancies seems unlikely. From the high-resolution micrographs of sample 3 in Fig. 3, though such structural defects were not clearly noticed, but importantly, it showed diamagnetic behaviour, which would go against the proposition.

We now consider the other source of ferromagnetism, namely the magnetic atoms revealed by SIMS (see Table 1). Here, there could be two extreme cases: the diluted magnetic scenario, where magnetic atoms enter as dopants, uniformly distributed over the MoS₂, which would imply the system is a chemically homogeneous alloy. This is certainly the most desirable case. And the second scenario is where the magnetic impurities are aggregated, forming a secondary phase of clusters.

From our TOF-SIMS experimental data, we have estimated the PM contributions (Supplementary Information). For that matter, we have assumed that every dopant contributes and behaves as a $J = 1/2$, $g = 2$ paramagnetic impurity. Given the density of dopants obtained from the chemical analysis, this model yields a magnetization per unit formula as a function of temperature and magnetic field. The resulting curves for samples 1 and 2 are shown as

plot 1a and 2a in Fig. 1c. This is subsequently compared with experimental extracted PM contributions shown by solid line curves in Fig. 1c. It is noted that the plots 1a and 1b have much higher saturation magnetization as compared to the experimental ones. Thus, in order to account for the paramagnetic signal observed in the experiments, it would be enough to assume that only 20% of the impurities are acting as paramagnetic centres.

In addition, we note that the saturation moment of the ferromagnetic component is around (40mBM) per Fe atom for sample 1 and (10mBM) per Fe atoms for sample 2, much smaller than (1) BM per Fe atom expected from most compounds. Therefore, the observed ferromagnetic signal is being generated by a few percent of the impurity atoms in the sample.

Thus, our results seem to suggest a scenario where a fraction of dopants even lesser than 1% are involved in the ferromagnetic order, and about one-fifth of the magnetic dopants are involved in the paramagnetic signal. Presumably magnetic impurities, such as Fe, are distributed all over the sample, as shown in Fig. 2b, and are likely candidates to account for the paramagnetic signal. In contrast, a diluted ferromagnetic phase that survives at room temperature requires a large density of magnetic dopants [51, 52], incompatible with our observations. Therefore, we claim that the most likely origin of the ferromagnetic signal is extrinsic from the well-distributed secondary phase of nano-clusters of Fe and other magnetic dopants, within a sea of distributed dopants, which result in paramagnetic signals.

Conclusions

In conclusion, we have carefully examined commercially available MoS₂ samples. Detailed characterization has been carried out in order to carefully understand the chemical composition, structure and morphology of the different samples. The origin of the magnetic behaviour has been traced to the presence of significant quantity of Fe and/or some other magnetic dopant elements present with the primary MoS₂.

This study demonstrates the presence of stable ferromagnetism at room temperature coming from a secondary phase of metallic clusters, mixed with the MoS₂ flakes which is different from dilute magnetic

alloying. We would especially like to highlight and caution the unintentional presence of the clusters within these materials, which need to be carefully accounted for in the study of diluted magnetic MoS₂, as well as in experiments reporting ferromagnetic order of other materials using MoS₂ as a substrate [53] in future experimental studies when reporting their magnetic behaviour. The unintentional presence of ferromagnetic clusters may lead to extrinsic ferromagnetic signals from typically diamagnetic samples and can easily be misinterpreted, to be intrinsic magnetic behaviour, if proper care is not taken.

Acknowledgements

The authors would like to thank the FCT-UT Austin project “Two dimensional magnetic semiconductors (2DMS): UTAPEXPL/NTec/0046/2017” for support of this research. One of the authors SS would like to thank DMRL, DRDO, Govt. of India, for granting permission to carry out this research work. The authors would like to acknowledge the SIMS characterization, carried out by Dr. Carmen Serra Rodríguez at C.A.C.T.I., University of Vigo, Spain. SS would also like to thank Dr. Jérôme Borme for useful discussions on XRD of the samples.

Supplementary Information: The online version contains supplementary material available at <http://doi.org/10.1007/s10853-021-05916-z>.

References

- [1] Mak KF, Lee C, Hone J et al (2010) Atomically thin MoS₂: a new direct-gap semiconductor. *Phys Rev Lett* 105:136805. <https://doi.org/10.1103/PhysRevLett.105.136805>
- [2] Molina-Sánchez A, Hummer K, Wirtz L (2015) Vibrational and optical properties of MoS₂: From monolayer to bulk. *Surf Sci Rep* 70:554–586. <https://doi.org/10.1016/j.surfrep.2015.10.001>
- [3] Krishnan U, Kaur M, Singh K et al (2019) A synoptic review of MoS₂: Synthesis to applications. *Superlattices Microstruct* 128:274–297. <https://doi.org/10.1016/j.spmi.2019.02.005>
- [4] Xiao D, Liu G-B, Feng W et al (2012) Coupled Spin and Valley Physics in Monolayers of MoS₂ and Other Group-VI Dichalcogenides. *Phys Rev Lett* 108:196802. <https://doi.org/10.1103/PhysRevLett.108.196802>
- [5] Catarina G, Have J, Fernández-Rossier J, Peres NMR (2019) Optical orientation with linearly polarized light in transition metal dichalcogenides. *Phys Rev B* 99:125405. <https://doi.org/10.1103/PhysRevB.99.125405>
- [6] Xu X, Yao W, Xiao D, Heinz TF (2014) Spin and pseudospins in layered transition metal dichalcogenides. *Nat Phys* 10:343–350. <https://doi.org/10.1038/nphys2942>
- [7] Kośmider K, González JW, Fernández-Rossier J (2013) Large spin splitting in the conduction band of transition metal dichalcogenide monolayers. *Phys Rev B Condens Matter Mater Phys* 88:245436. <https://doi.org/10.1103/PhysRevB.88.245436>
- [8] Mak KF, Shan J, Ralph DC (2019) Probing and controlling magnetic states in 2D layered magnetic materials. *Nat Rev Phys* 1:646–661. <https://doi.org/10.1038/s42254-019-0110-y>
- [9] Gibertini M, Koperski M, Morpurgo AF, Novoselov KS (2019) Magnetic 2D materials and heterostructures. *Nat Nanotechnol* 14:408–419. <https://doi.org/10.1038/s41565-019-0438-6>
- [10] Huang B, Clark G, Navarro-Moratalla E et al (2017) Layer-dependent ferromagnetism in a van der Waals crystal down to the monolayer limit. *Nature* 546:270–273. <https://doi.org/10.1038/nature22391>
- [11] Zhang WB, Qu Q, Zhu P, Lam CH (2015) Robust intrinsic ferromagnetism and half semiconductivity in stable two-dimensional single-layer chromium trihalides. *J Mater Chem C* 3:12457–12468. <https://doi.org/10.1039/c5tc02840j>
- [12] Lado JL, Fernández-Rossier J (2017) On the origin of magnetic anisotropy in two dimensional CrI₃. *2D Mater* 4:35002. <https://doi.org/10.1088/2053-1583/aa75ed>
- [13] Gong C, Li L, Li Z et al (2017) Discovery of intrinsic ferromagnetism in two-dimensional van der Waals crystals. *Nature* 546:265–269. <https://doi.org/10.1038/nature22060>
- [14] Song T, Cai X, Tu MWY, et al (2018) Giant tunneling magnetoresistance in spin-filter van der Waals heterostructures. *Science* (80-) 360:1214–1218. <https://doi.org/https://doi.org/10.1126/science.aar4851>
- [15] Kong T, Stolze K, Timmons EI et al (2019) VI₃ —a New Layered Ferromagnetic Semiconductor. *Adv Mater* 31:1–7. <https://doi.org/10.1002/adma.201808074>
- [16] Freitas DC, Weht R, Sulpice A et al (2015) Ferromagnetism in layered metastable 1T-CrTe₂. *J Phys Condens Matter* 27:176002. <https://doi.org/10.1088/0953-8984/27/17/176002>
- [17] Ahn EC (2020) 2D materials for spintronic devices. *npj 2D Mater Appl* 4:1–14. <https://doi.org/10.1038/s41699-020-0152-0>

- [18] Samarth N, Furdyna JK (1988) Diluted Magnetic Semiconductors. *MRS Bull* 13:32–36. <https://doi.org/10.1557/S0883769400065477>
- [19] Ohno H, Shen A, Matsukura F et al (1996) (Ga, Mn)As: A new diluted magnetic semiconductor based on GaAs. *Appl Phys Lett* 69:363–365. <https://doi.org/10.1063/1.118061>
- [20] MacDonald AH, Schiffer P, Samarth N (2005) Ferromagnetic semiconductors: moving beyond (Ga, Mn)As. *Nat Mater* 4:195–202. <https://doi.org/10.1038/nmat1325>
- [21] Dietl T, Ohno H (2014) Dilute ferromagnetic semiconductors: Physics and spintronic structures. *Rev Mod Phys* 86:187–251. <https://doi.org/10.1103/RevModPhys.86.187>
- [22] Wolf SA, Awschalom DD, Buhrman RA, et al (2001) Spintronics: A spin-based electronics vision for the future. *Science* (80-) 294:1488–1495. <https://doi.org/https://doi.org/10.1126/science.1065389>
- [23] Han W (2016) Perspectives for spintronics in 2D materials. *APL Mater* 4:32401. <https://doi.org/10.1063/1.4941712>
- [24] Tongay S, Varnoosfaderani SS, Appleton BR et al (2012) Magnetic properties of MoS₂: Existence of ferromagnetism. *Appl Phys Lett* 101:123105. <https://doi.org/10.1063/1.4753797>
- [25] Sun B, Li QL, Chen P (2014) Room-temperature ferromagnetism of single-crystalline MoS₂ nanowires. *Micro Nano Lett* 9:468–470. <https://doi.org/10.1049/mnl.2014.0201>
- [26] Zhang J, Soon JM, Loh KP et al (2007) Magnetic molybdenum disulfide nanosheet films. *Nano Lett* 7:2370–2376. <https://doi.org/10.1021/nl071016r>
- [27] Shidpour R, Manteghian M (2010) A density functional study of strong local magnetism creation on MoS₂ nanoribbon by sulfur vacancy. *Nanoscale* 2:1429–1435. <https://doi.org/10.1039/b9nr00368a>
- [28] Xu W, Yan S, Qiao W (2018) Magnetism in monolayer 1T-MoS₂ and 1T-MoS₂H tuned by strain. *RSC Adv* 8:8435–8441. <https://doi.org/10.1039/c7ra10304b>
- [29] Cai L, He J, Liu Q et al (2015) Vacancy-induced ferromagnetism of MoS₂ nanosheets. *J Am Chem Soc* 137:2622–2627. <https://doi.org/10.1021/ja5120908>
- [30] Lin X, Ni J (2014) Charge and magnetic states of Mn-, Fe-, and Co-doped monolayer MoS₂. *J Appl Phys* 116:44311. <https://doi.org/10.1063/1.4891495>
- [31] Fan XL, An YR, Guo WJ (2016) Ferromagnetism in transitional metal-doped MoS₂ monolayer. *Nanoscale Res Lett* 11:1–10. <https://doi.org/10.1186/s11671-016-1376-y>
- [32] Mishra R, Zhou W, Pennycook SJ et al (2013) Long-range ferromagnetic ordering in manganese-doped two-dimensional dichalcogenides. *Phys Rev B Condens Matter Mater Phys* 88:144409. <https://doi.org/10.1103/PhysRevB.88.144409>
- [33] Li Q, Zhao X, Deng L et al (2020) Enhanced valley zeeman splitting in Fe-doped monolayer MoS₂. *ACS Nano* 14:4636–4645. <https://doi.org/10.1021/acsnano.0c00291>
- [34] Song B, Yun SJ, Jiang J, et al (2020) Evidence of itinerant holes for long-range magnetic order in tungsten diselenide semiconductor with vanadium dopants. 1–19
- [35] Jimenez VO, Pham YTH, Liu M, et al (2020) Light-controlled room temperature ferromagnetism in vanadium-doped tungsten diselenide semiconducting monolayers. 1–21
- [36] Pham YTH, Liu M, Jimenez VO, et al (2020) Tunable Ferromagnetism and Thermally Induced Spin Flip in Vanadium-doped Tungsten Diselenide Monolayers at Room Temperature
- [37] Zhang F, Zheng B, Sebastian A, et al (2020) Monolayer Vanadium-doped Tungsten Disulfide: A Room-Temperature Dilute Magnetic Semiconductor. 1–38
- [38] Guguchia Z, Kerelsky A, Edelberg D et al (2018) Magnetism in semiconducting molybdenum dichalcogenides. *Sci Adv* 4:1–9. <https://doi.org/10.1126/sciadv.aat3672>
- [39] Suh J, Park TE, Lin DY et al (2014) Doping against the native propensity of MoS₂: Degenerate hole doping by cation substitution. *Nano Lett* 14:6976–6982. <https://doi.org/10.1021/nl503251h>
- [40] Hallam T, Monaghan S, Gity F et al (2017) Rhenium-doped MoS₂ films. *Appl Phys Lett* 111:203101. <https://doi.org/10.1063/1.4995220>
- [41] Sigiuro M, Huang YS, Ho CH et al (2015) Influence of rhenium on the structural and optical properties of molybdenum disulfide. *Jpn J Appl Phys* 54:6. <https://doi.org/10.7567/JJAP.54.04DH05>
- [42] Ko TS, Chen ZW, Lin DY et al (2017) Observation of persistent photoconductivity in Ni-doped MoS₂. *Jpn J Appl Phys* 56:4–8. <https://doi.org/10.7567/JJAP.56.04CP09>
- [43] Kao CW, Yang CC, Kao HC et al (2018) Role of Fe-doping effect in 2-D MoS₂ magnetic semiconductor. *IEEE Trans Magn* 54:2018–2020. <https://doi.org/10.1109/TMAG.2018.2829267>
- [44] Singh MK, Chettri P, Tripathi A et al (2018) Defect mediated magnetic transitions in Fe and Mn doped MoS₂. *Phys Chem Chem Phys* 20:15817–15823. <https://doi.org/10.1039/c8cp02882f>
- [45] Ahmed S, Ding X, Bao N et al (2017) Inducing high coercivity in MoS₂ nanosheets by transition element doping. *Chem Mater* 29:9066–9074. <https://doi.org/10.1021/acs.chemmater.7b02593>
- [46] Zhou J, Lin J, Sims H et al (2020) Synthesis of Co-Doped MoS₂ monolayers with enhanced valley splitting. *Adv Mater* 32:1–8. <https://doi.org/10.1002/adma.201906536>
- [47] Fu S, Kang K, Shayan K et al (2020) Enabling room temperature ferromagnetism in monolayer MoS₂ via in situ iron-

- doping. *Nat Commun* 11:2034. <https://doi.org/10.1038/s41467-020-15877-7>
- [48] Matsubayashi K, Maki M, Moriwaka T et al (2003) Extrinsic origin of high-temperature ferromagnetism in CaB₆. *J Phys Soc Japan* 72:2097–2102. <https://doi.org/10.1143/JPSJ.72.2097>
- [49] Sepioni M, Nair RR, Tsai I-L et al (2012) Revealing common artifacts due to ferromagnetic inclusions in highly oriented pyrolytic graphite. *EPL Europhys Lett* 97:47001. <https://doi.org/10.1209/0295-5075/97/47001>
- [50] Xia B, Yang Y, Ma J et al (2017) Adjustable ferromagnetic behavior in iron-doped two-dimensional MoS₂ multilayer nanosheets. *Appl Phys Express* 10:093002. <https://doi.org/10.7567/APEX.10.093002>
- [51] Wang Y, Li S, Yi J (2016) Electronic and magnetic properties of Co doped MoS₂ monolayer. *Sci Rep* 6:1–9. <https://doi.org/10.1038/srep24153>
- [52] Dietl T, Ohno H, Matsukura F, et al (2000) Zener Model Description of Ferromagnetism in Zinc-Blende Magnetic Semiconductors. *Science* (80-) 287:1019–1022. <https://doi.org/https://doi.org/10.1126/science.287.5455.1019>
- [53] Bonilla M, Kolekar S, Ma Y et al (2018) Strong room-temperature ferromagnetism in VSe₂ monolayers on van der Waals substrates. *Nat Nanotechnol* 13:289–293. <https://doi.org/10.1038/s41565-018-0063-9>

Publisher's Note Springer Nature remains neutral with regard to jurisdictional claims in published maps and institutional affiliations.